

Unveiling the microscopic dynamics of the charge density wave transition in monolayer VX_2 ($X = S, Te$)

Yuxuan Chen,¹ Chao Liang,¹ Jian Yuan,¹ Biao Wang,^{1,*} and Huashan Li^{1,2,3,†}

¹*School of Physics, Sun Yat-Sen University, Guangzhou 510275, China*

²*Guangdong Provincial Key Laboratory of Magnetoelectric Physics and Devices, School of Physics, Sun Yat-sen University, Guangzhou 510275, China*

³*School of Materials Science and Engineering, Dongguan University of Technology, Dongguan 523808, China*

 (Received 20 November 2023; revised 18 February 2024; accepted 25 March 2024; published 25 April 2024)

Charge density waves (CDWs) in two-dimensional materials have received great attention due to their intriguing properties, yet the microscopic evolution process of CDW transition and its impact on charge transport remain to be fully understood. Herein we employed density-functional theory calculations to ascertain the richness of CDW phases in VX_2 ($X = S, Te$) originated from electron-phonon coupling. Reversible transitions between the normal and CDW phases are directly simulated with *ab initio* molecular dynamics, indicating that the formation of CDW phase is a rapid nucleation process. The corresponding microscopic dynamic processes involve the formation, flipping, translation, and aggregation of characteristic patterns, which are driven by the soft phonon modes. Modifications of electrical conductivity in CDW phase transition are found to stem from the varying orientation and location distributions of relevant wave functions. The revealed dynamic mechanism opens an opportunity for the control of CDW phase transition that is crucial to its applications in logical circuits and neural networks.

DOI: [10.1103/PhysRevB.109.L140105](https://doi.org/10.1103/PhysRevB.109.L140105)

Introduction. Charge density waves (CDWs) are important broken-symmetry states widely existing in the rich phase diagrams of correlated electron systems [1–4]. A variety of commensurate and incommensurate CDW states have been found in transition-metal dichalcogenides (TMDCs) [5–9]. Ultrafast and reversible phase transitions were observed in TaS_2 under femtosecond laser irradiation, which highlights the potential of CDW in photodetection and high-speed non-volatile memory devices [10–12]. Recently, the family of vanadium dichalcogenides VX_2 ($X = S, Se, Te$) attracted much attention due to their intriguing properties, such as the coexistence of multiple phases, ferromagnetic order, high phase-transition temperature, and dimension-dependent phase transition [13–18]. For monolayer (ML) VS_2 , $7 \times \sqrt{3}$, $9 \times \sqrt{3}$ [15], and $\sqrt{21} \times \sqrt{3}$ [19] CDW structures were detected by scanning tunneling microscope, with the transition temperature estimated as 400 K [14]. In contrast, ML $T-VTe_2$ has a 4×4 CDW superlattice at low temperature, while the ML $H-VTe_2$ is found to exhibit a robust $2\sqrt{3} \times 2\sqrt{3}$ CDW superlattice with a transition temperature above 450 K [20].

Extensive theoretical studies have been conducted to elucidate the origin of CDWs. The analyses of electronic structure and electron-phonon interactions demonstrated that the CDWs in two-dimensional materials mainly arise from the electron-phonon coupling (EPC) or Fermi-surface nesting effects [21–25]. Through density-functional theory (DFT) calculations, various energetically favorable CDW structures

as well as critical phonon modes responsible for the phase transitions were successfully predicted [26,27]. In addition, the formation of multicenter bonds and the enhancement of p - d orbital hybridization were analyzed from the perspective of electronic origin to investigate the structural modulations in TMDC systems [26,28–33]. While most of the existing literature focused on investigating the electronic structure and phonon spectrum, only a few theoretical works were devoted to exploring the CDW-related phase-transition process, and all of them considered system properties at several discrete temperatures [34–36]. Specifically, *ab initio* molecular dynamics (AIMD) were applied to determine the energetically favorable microscopic structures [34] and the dynamics of adsorbed atoms [35]. Joint AIMD and path-integral MD simulations were performed to unveil the finite-temperature effects and nuclear quantum effects [36].

The profound investigation of CDW-related phase-transition processes is restricted by the insufficient temporal resolution in experiment and the limited space–timescale accessed by AIMD simulations. Spatial inhomogeneity has been detected by experiments, which demonstrated that the CDW phase transition proceeds through a nucleation mode [13]. Although atomic-scale evolution can be probed with DFT calculations, the continuous CDW nucleation process has never been observed due to the insufficient simulation period [37,38]. Recently, machine-learned force fields (MLFFs) were developed to accelerate the AIMD simulations by orders of magnitude [39,40], yet they have not been applied in CDW phase-transition research. So far, the microscopic evolution process of CDW transition and its correlation with soft phonon modes remains to be fully understood. In addition, the

*Corresponding author: wangbiao@mail.sysu.edu.cn

†Corresponding author: lihsh25@mail.sysu.edu.cn

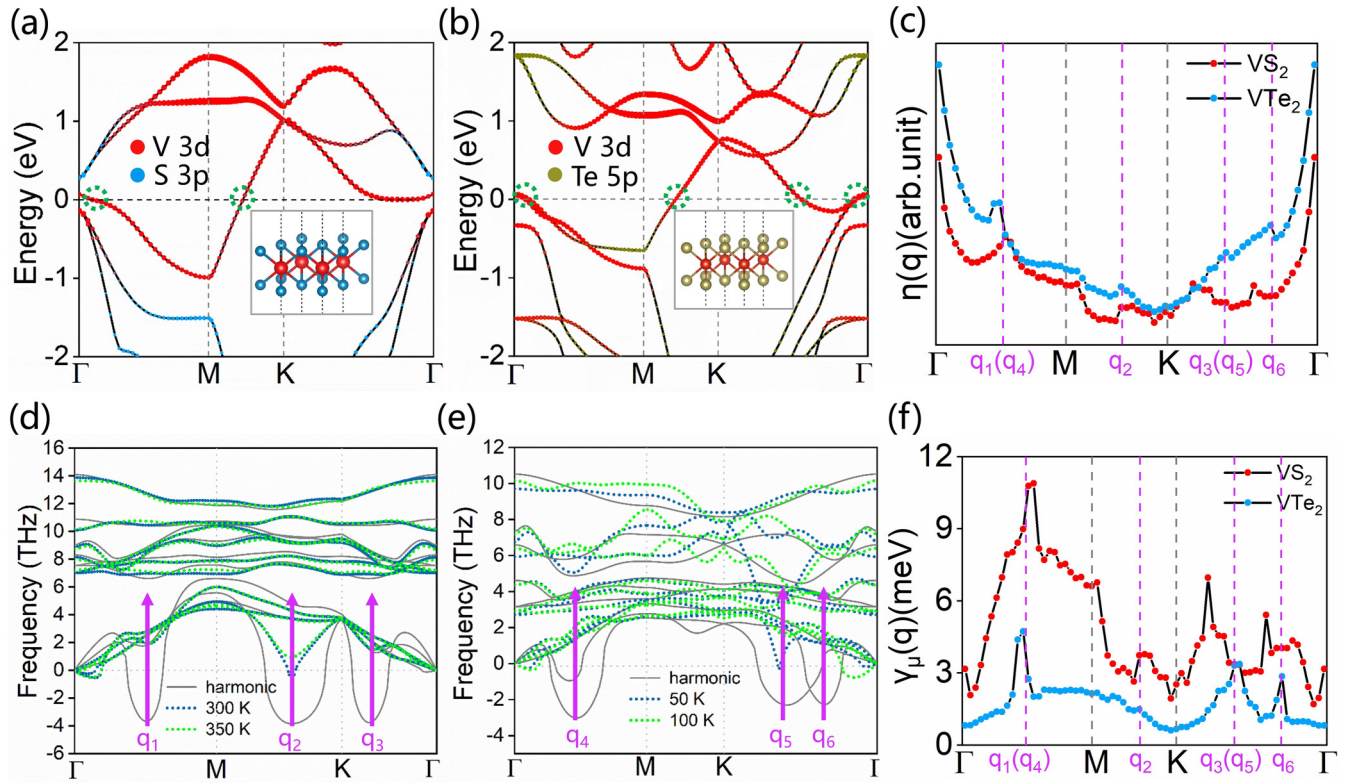


FIG. 1. Electronic and phononic structures of VS_2 and VTe_2 . The projected band structure of (a) VS_2 and (b) VTe_2 . The electron orbits of V $3d$, S $3p$, and Te $5p$ are presented in red, blue, and brown dots, respectively, with the dot size denoting the orbital weight. Atomic structures of VS_2 and VTe_2 are shown in the inset. (c) Fermi-nesting function $\eta(q)$ and (f) phonon linewidth $\gamma_\mu(q)$ of VS_2 and VTe_2 evaluated to probe the electron-phonon interactions. The q vectors of unstable phonon modes are represented by the purple dashed lines. Phonon dispersions of (d) VS_2 and (e) VTe_2 . Harmonic phonon dispersions are represented with gray solid lines, while anharmonic phonon dispersions at different temperatures are displayed with colored dotted lines.

order parameters to quantify the CDW phase transition and the effects of structural change on charge-transport property are still unclear. Nevertheless, such information would enable the optimization of CDW phase transition and thus is essential for the applications of logic circuits [41], nonvolatile memory [42], and oscillatory neural networks [43].

In this work, we systemically investigated the underlying physics of diverse CDW orders as well as the microscopic dynamic process of CDW transition in ML $1T$ - VS_2 and $1T$ - VTe_2 (abbreviated to VS_2 and VTe_2) by joint DFT and AIMD methods. The calculated electronic and phononic structures imply that electron-phonon coupling is the main origin of CDW transitions. Cooling and heating simulations with AIMD unveil the atomic-scale evolution during the reversible transition between normal and CDW phases. A rapid nucleation mechanism strongly associated with phonon vibrations is proposed to describe the formation of CDW phase. This research advances the understanding of CDW transition in two-dimensional materials and provides insights for the development of electronic devices.

Results and Discussion. Electronic and phononic properties. Electronic and phononic structures were comprehensively investigated by DFT simulations to unveil the origin of CDWs in VS_2 and VTe_2 monolayers (Fig. 1). Our testing results (see Fig. S1) indicate that using the generalized gradient approximation (GGA)+ U (V $3d = 2.5$ eV)

functional is more suitable for describing the CDW properties of VX_2 ($X = \text{S}, \text{Te}$) than the local density approximation (LDA)+ U functional. The optimized structure of normal-state (NS) VS_2 and VTe_2 possesses a $P\bar{3}m1$ space group with lattice parameters of $a = b = 3.11$ Å and $a = b = 3.44$ Å, respectively. The projected band structure [Figs. 1(a) and 1(b)] indicates that both VS_2 and VTe_2 are metallic. For VS_2 , two energy bands pass through the Fermi level (E_F), with the crossing near the Γ point and $2/5$ along the M - K direction. The VTe_2 has an additional crossing point around $1/2$ along the Γ - K direction compared to the VS_2 . The energy bands near E_F in both VS_2 and VTe_2 are mainly contributed by the V $3d$ orbitals, which justifies our focus on the V atoms in dynamic analyses. The calculated harmonic phonon dispersion is displayed in Figs. 1(d) and 1(e). The three dominant instabilities at wave vector $q_1 = 1/2\Gamma M$, $q_2 = 3/5MK$, and $q_3 \approx 3/5\Gamma K$ indicate the dynamical instability of NS. The q vectors corresponding to the Kohn anomalies within the first Brillouin zone (BZ) can be translated into the lattice vectors of the potential CDW structures in real space [44,45]. For VS_2 , the instability at q_1 is associated with a 4×4 supercell (Fig. S2(f) in the Supplemental Material (SM) [46]); Refs. [47–73], while the combination of q_2 and q_3 may lead to a $\sqrt{7} \times \sqrt{3}$ modulation. Likewise, the soft phonon modes of VTe_2 at $q_4 = 1/2\Gamma M$, $q_5 = 3/5\Gamma K$, and $q_6 = 1/3\Gamma K$ are related to the 4×4 , $2\sqrt{3} \times 2\sqrt{3}$, and 6×6 supercells (Fig. S3) [74].

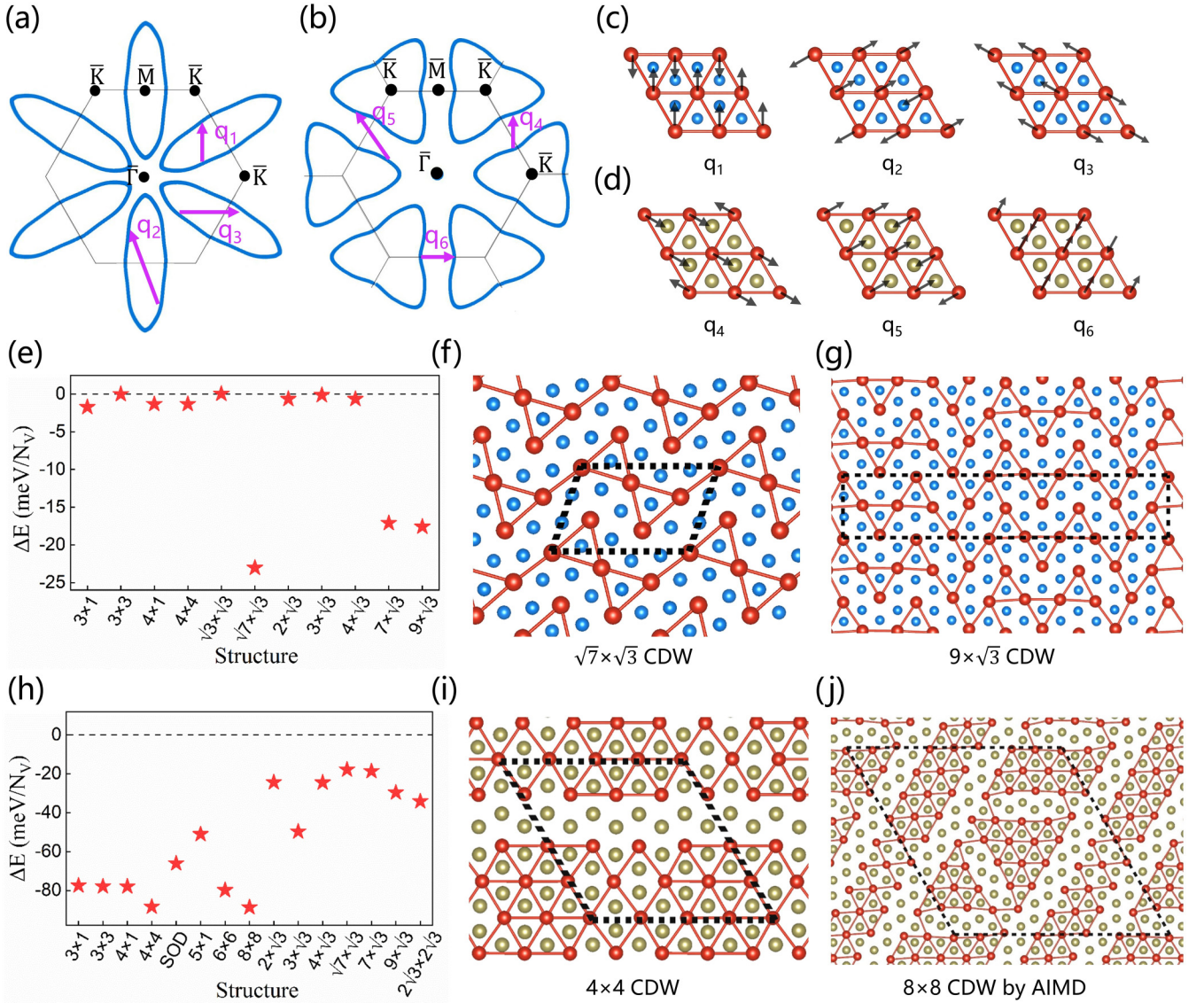


FIG. 2. Analyses of potential CDW phases in VS_2 and VTe_2 . Two-dimensional Fermi surfaces of NS: (a) VS_2 and (b) VTe_2 on the (001) surface plane, along with the CDW vectors indicated by red arrows. Schematic illustration of the relative atomic motion driven by soft phonon modes associated with the (c) q_1 , q_2 , and q_3 vectors for VS_2 as well as the (d) q_4 , q_5 , and q_6 vectors for VTe_2 . Formation energies ΔE of the potential CDW structures in (e) VS_2 and (h) VTe_2 . Schematic diagrams of CDW structures with the lowest ΔE : (f) $\sqrt{7} \times \sqrt{3}$ and (g) $9 \times \sqrt{3}$ CDW in VS_2 ; (i) 4×4 and (j) 8×8 CDW by AIMD in VTe_2 . Red, blue, and brown spheres denote the V, S, and Te atoms, respectively. The black dashed parallelograms show periodicities of CDW structures. The cutoff lengths for the V–V bonds in VS_2 and VTe_2 are 3.11 and 3.44 Å, respectively.

The transition temperature between the normal and CDW phases was estimated through looking into the phonon dispersion and identifying the temperature at which soft modes vanish [75–77]. The harmonic phonon dispersions were attained by the PHONOPY code [78], and the anharmonic phonon dispersions at various temperatures were calculated by the DYNAPHOPY code [79]. As the temperature increases, the imaginary frequencies around all q vectors vanish above $T_{\text{CDW}} \approx 310$ K [Fig. 1(d)], which is consistent with the experimental speculation of $T_{\text{CDW}} \approx 400$ K [14] and not far above room temperature [15]. Likewise, the T_{CDW} of VTe_2 is estimated at 100 K based on the phonon spectra [Fig. 1(e)], which is close to the experimental value of 135 K [80]. The higher transition temperature of VS_2 compared to VTe_2 may

be explained by the stronger V–S bonds that stabilize the CDW phase.

Formation mechanism of diverse CDW. To understand the phase-transition mechanism, we comprehensively analyzed the effects of Fermi-surface nesting and electron-phonon coupling. There are six cigar-shaped electron pockets at the Fermi surface of VS_2 , which are centered at M points as shown in Fig. 2(a). Regarding VTe_2 , the Fermi surface includes six triangle pockets centered at K points [Fig. 2(b)]. Partial nesting characters are observed in both Fermi surfaces, as illustrated by their connections with the soft phonon modes. To unveil the impact of Fermi-surface nesting on stabilizing the CDW state, the unfolded band structures were computed for representative CDWs in VS_2 [Figs. S4(a)–S4(d)]. Multiple minor gap

openings emerge in the $\sqrt{7} \times \sqrt{3}$ CDW compared to the NS, while weak tearing effect appears only at the $2/5$ along the M - K direction in $2 \times \sqrt{3}$ CDW. The situation for VTe_2 becomes slightly different [Figs. S4(e)–S4(h)]. In the $\sqrt{7} \times \sqrt{3}$ CDW, we observe three slight tears at Γ , $1/2 \Gamma M$, and M points, which give rise to sharp cone-shaped energy bands. Furthermore, the 4×1 and 4×4 CDWs exhibit the weak tearing effects at the $2/5$ position along the M - K direction. The results indicate that the formation of CDW has a certain degree of Fermi-surface nesting. In order to estimate the contributions from Fermi-surface nesting and electron-phonon coupling, the Fermi-nesting function $\eta(\mathbf{q})$ and phonon linewidth $\gamma(\mathbf{q})$ were computed by the following equations [37,81]:

$$\eta(\mathbf{q}) = \frac{1}{N} \sum_{nm'} \sum_{\mathbf{k}}^{\text{1BZ}} \delta(\varepsilon_{n,\mathbf{k}+\mathbf{q}} - \varepsilon_F) \delta(\varepsilon_{n\mathbf{k}} - \varepsilon_F), \quad (1)$$

$$\gamma_{\mu}(\mathbf{q}) = \frac{2\pi w_{\mu}(\mathbf{q})}{N} \sum_{nm'} \sum_{\mathbf{k}}^{\text{1BZ}} |g_{n,\mathbf{k}+\mathbf{q},n\mathbf{k}}^{\mu}|^2 \delta(\varepsilon_{n,\mathbf{k}+\mathbf{q}} - \varepsilon_F) \times \delta(\varepsilon_{n\mathbf{k}} - \varepsilon_F), \quad (2)$$

wherein $\varepsilon_{n\mathbf{k}}$ represents the energy of band n at wave vector \mathbf{k} , ε_F denotes the Fermi energy, N refers to the total number of k points summed over the first Brillouin zone (1BZ). The nesting function peaks for \mathbf{q} signify the connection of nested regions in the Fermi surface, thereby serving as an indicator of whether the instability arises solely from electronic factors. The equation for $\gamma_{\mu}(\mathbf{q})$ is constructed from the nesting function by incorporating the weighting function of electron-phonon matrix elements, which reflect the impact of electron-phonon interactions on the system's instability. As shown in Fig. 1(c), the nesting function has local peaks at around all \mathbf{q} vectors (except q_3) of soft phonon modes, but the associated peak values are much lower than the highest peak at Γ point. In contrast, the phonon linewidth reaches its peak at these \mathbf{q} vectors, with the peak value at $q_1(q_4)$ much higher than the value at Γ point [Fig. 1(f)]. Therefore, the intrinsic CDW orders of VS_2 and VTe_2 are mainly driven by EPC rather than Fermi-surface nesting, which is consistent with the previous finding on VSe_2 [27,82].

The energetically favorable CDW orders in VS_2 and VTe_2 were determined by predicting the formation energies ΔE of different possible CDW structures as summarized in Figs. 2(e) and 2(h) (detailed structural information of various CDWs including lattice constants, bond lengths, and bond angles were documented in Table S1). The results suggest that the $\sqrt{7} \times \sqrt{3}$, $7 \times \sqrt{3}$ [Fig. S2(g)], and $9 \times \sqrt{3}$ CDW are mostly likely to form in VS_2 , which is consistent with previous experiments [15]. Other CDW, such as the $2 \times \sqrt{3}$ structure, will spontaneously aggregate and transform into the $\sqrt{7} \times \sqrt{3}$ structure in our AIMD simulation [Fig. S7(c)]. Compared to the limited energetically favorable CDW structures in VS_2 , all tested CDW structures in VTe_2 possess large negative formation energies, indicating the potential existence and mixture of various CDWs. Among them, 8×8 , 4×4 [Fig. 2(i)], 4×1 [Fig. S3(i)], and 3×3 [Fig. S3(k)] stripes are the most energetically favorable CDW structures, which have lower ΔE than the Stars of David and $2\sqrt{3} \times 2\sqrt{3}$ structures [Fig. S3(f)]. The 8×8 CDW structure with lowest ΔE is

discovered by the following AIMD simulation. Since the stability of CDW is highly sensitive to substrate and doping, all the above CDW structures may be observed in experiments with appropriate environmental conditions [27,83–85]. Furthermore, we performed the Integrated crystal orbital bond index (ICOBI) analyses on all potential V–V–V bonds in both VS_2 and VTe_2 CDW. The results revealed that the majority of these bonds exhibit high ICOBI values, indicating the existence of three-center (3c) bonds, as shown in Fig. 3. Such multicenter bonds stabilized the ribbon and zigzag chains of the V ions through the σ interactions between in-plane t_{2g} orbitals, as explained by previous theoretical studies [86–88]. In addition, the enhancement of p - d hybridization within the V–S(Te) bonds and p - p hybridization within the Te–Te bonds play an important role in CDW stabilization, as evidenced by the reduced ICOHP values in the CDW phases compared to the normal phases. (See the S5 and S6 in the SM for more detailed results and discussions.)

Microscopic dynamic process of CDW phase transition. To elucidate the underlying microscopic evolution of the CDW phase transition, we employed MLFFs-AIMD to simulate the cooling (450 to 0 K) and heating (0 to 450 K) processes [Figs. 4(a) and 4(b)]. Initially, a 5-ps equilibrium simulation at 450 K was conducted to obtain a randomly perturbed configuration. Subsequently, the structure was gradually cooled down to 0 K with a rate of 5 ps/K. Finally, the 0 K structure was further heated back up to 450 K using the same rate. Note that the cooling and heating rates in our simulation are sufficiently slow for the observation of crystalline process, but still too fast for determining the phase-transition temperature. Among the CDWs observed in experiments, the $9 \times \sqrt{3}$ and 4×4 structures possess the lowest calculated formation energy in VS_2 and VTe_2 , respectively. The $9 \times \sqrt{3}$ and 8×8 supercells corresponding to these CDW structures were thus adopted for VS_2 and VTe_2 in AIMD simulations.

During the cooling process, both the VS_2 and VTe_2 supercells gradually evolve from the disordered NS to the CDW structures [Figs. 5(a)–5(h)]. The 0 K structures acquired from the AIMD simulations are identical with those obtained by DFT optimizations. During the heating process, the CDW structures vanish and the disordered NS structures recover. The above results indicate that the reversible transitions between the NS and CDW phases have been appropriately captured by the AIMD simulations. For quantitatively describing the phase-transition process, order parameters may be introduced to characterize the regulation of atomic structure. Nevertheless, traditional order parameters, such as radial distribution function and coordination number, exhibit tiny changes during CDW phase transition and thus cannot be applied to our system. An alternative order parameter of the maximum distance of V–V along the Z direction (d_{max}) was introduced to trace the structural distortion evolution as shown in Fig. 4(c). The d_{max} value exhibits a notable variation in regions surpassing the threshold of T_{CDW} . Conversely, in regions below the T_{CDW} , d_{max} demonstrates an approximately linear decline, indicating a gradual reduction in the distortion of the V–V layer towards the formation of CDW structure [89,90]. In addition, special order parameters were defined to measure the global pattern alignment, including the number

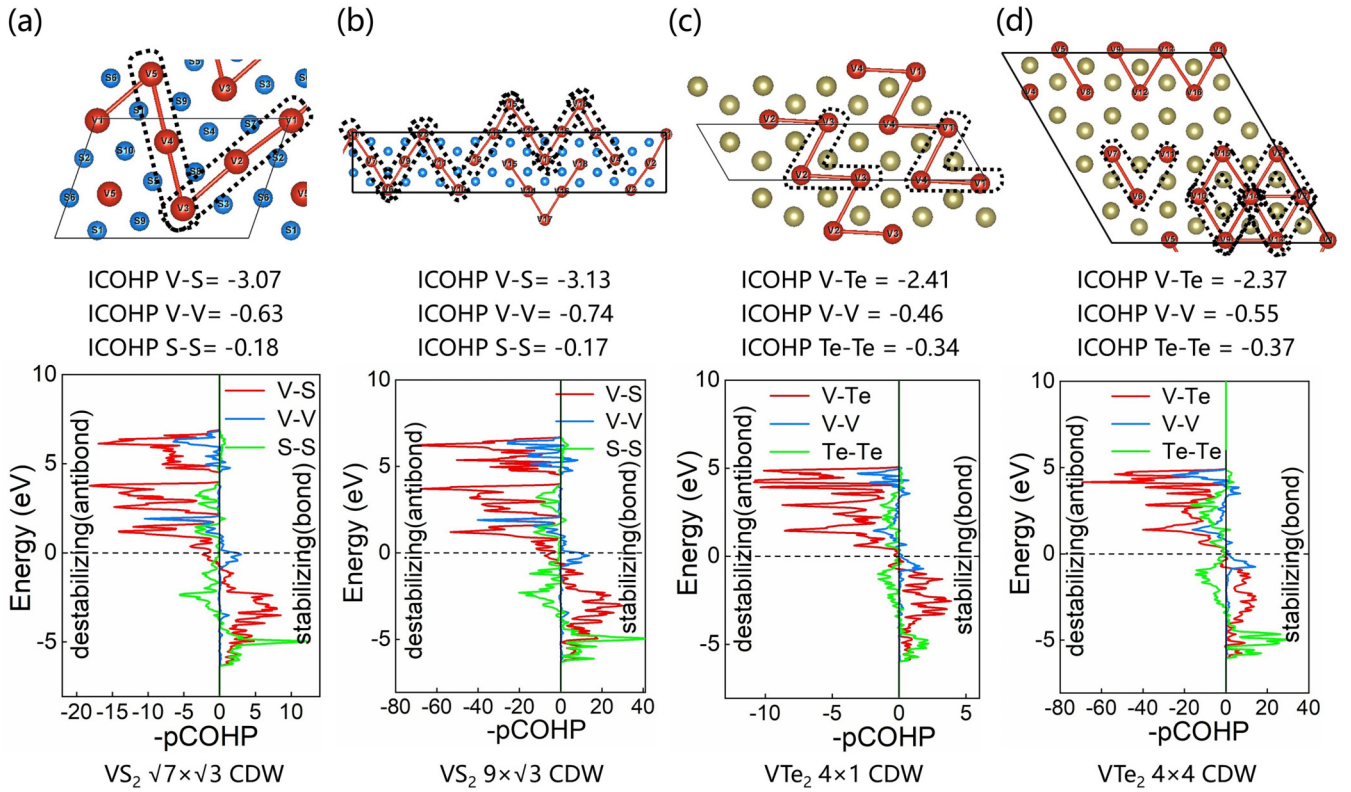


FIG. 3. Schematic illustration of the multicenter bonding and the p - d hybridization in CDW. The atomic structure and corresponding Integrated crystal orbital Hamilton population (ICOHP) in (a) $\text{VS}_2 \sqrt{7} \times \sqrt{3}$, (b) $\text{VS}_2 9 \times \sqrt{3}$ CDW, (c) $\text{VTe}_2 4 \times 1$, and (d) $\text{VTe}_2 4 \times 4$ CDW, respectively. Note that in order to highlight the three-center bonds, the V-V cutoff is shrunk to 3.05 Å in VS_2 and 3.25 Å in VTe_2 . The three-center (3c) bonds with high values of ICOBI are highlighted with black dashed boxes.

of butterfly shapes in VS_2 and the number of hexagons in VTe_2 [Figs. 4(d) and 4(e)]. Overall, the number of characteristic structures gradually increases with decreasing temperature, which demonstrates a continuous nature of the phase transition.

To understand the principle that governs the atomic motion, we conducted a comprehensive analysis of the structural changes during the AIMD cooling process, with the representative structural evolutions shown in Fig. 5. Consistent with previous experimental studies, the results suggest that the formations of CDW in both VS_2 and VTe_2 are rapid nucleation processes. Their initial nuclei are the butterfly shape with five V atoms and the hexagon shape with seven V atoms, respectively. The dynamic process in VS_2 primarily involves the formation, flipping, translation, and aggregation of butterfly-shaped structures. According to the calculated patterns of vibration modes [Fig. 2(c)], the soft phonon mode q_2 is responsible for the twisting of each V atom row, while the phonon mode q_3 is related to the relative motion between neighboring V-atom rows. The combination of these soft phonon modes may swiftly drive the flipping and translation of butterfly-shaped structure as schematically illustrated in Fig. 5. At the initial stage, the nuclei of a single butterfly shape [Fig. 5(a)] gradually grow to an entire strip of neatly aligned butterfly shapes [Fig. 5(b)]. Subsequently, another butterfly strip parallel to the first one appears, and the first strip flips as a whole to adjust the distance between the two

strips [Fig. 5(c)]. Eventually, the two butterfly strips and the intermediate V-shaped structure merge into a unified CDW pattern [Fig. 5(d)].

Regarding the phase transition in VTe_2 , the nucleation initializes from a hexagonal pattern with the highest coordination number [Fig. 5(e)]. Fast translation and expansion of hexagonal pattern may be driven by the soft phonon mode q_4 , which leads to distance fluctuation between neighboring V-atom rows [Fig. 5(f)]. As the temperature decreases, some hexagons agglomerate to form stripe patterns, while the reverse process can also occur to generate hexagons at different locations. With further reduction in temperature, the triangular agglomerates become more stable. These triangular patterns agglomerate can flip and move through the V-V connection exchanged with the neighboring hexagonal patterns, as facilitated by the soft phonon mode [Fig. 5(g)]. Once the stripe regions at the top and bottom of the triangle form, the system reaches a stable state such that the structure undergoes no further significant changes [Fig. 5(h)]. The cooling process is simulated with different initial structures to verify the robustness of the above dynamic process (Fig. S8). Furthermore, the CDW dynamics of VS_2 under mechanical strain were examined by simulations as illustrated in Fig. S9. Compressive strain makes it more challenging for periodic atomic displacement to occur and ultimately inhibits the transformation into a CDW structure at low temperature. Conversely, the impact of

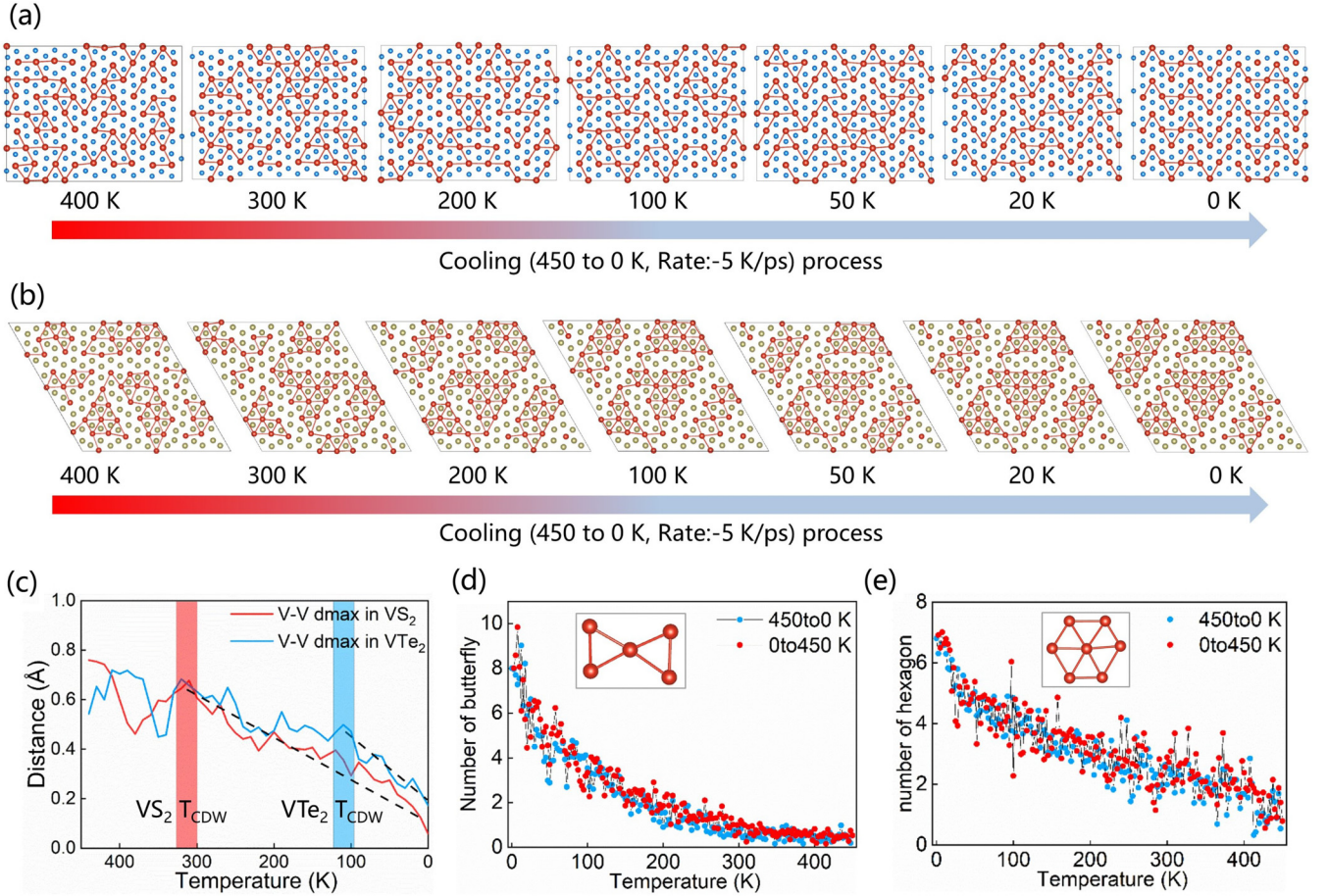


FIG. 4. Microscopic evolutions of CDW phase transitions revealed by AIMD simulations. The variations of atomic structure during the AIMD cooling and heating processes for (a) VS₂ and (b) VTe₂. (c) The maximum distances of V-V along the Z direction during the AIMD cooling processes as a function of temperature for VS₂ and VTe₂. Custom order parameters as a function of temperature for (d) VS₂ and (e) VTe₂. The red and blue dotted lines represent the AIMD heating and cooling processes, respectively. Each dot represents the average value of adjacent 100 structures during AIMD.

tensile strain is relatively weak, and the CDW structures can establish under 4% tensile strain with slight change of periodic pattern.

The impact of CDW phase transition on charge transport is explored via estimating the electrical conductivities of representative CDW structures by the BOLTZTRAP2 [91] code. Consistent with previous experiments [14,80,92], the predicted conductivities of CDWs in both VS₂ and VTe₂ are substantially lower than those of the normal phases [Figs. 5(i) and 5(j)]. To understand the distinct conductivities of different CDW and normal phases, we calculated the relevant projected density of states (PDOS) of V 3d orbitals (Fig. S11) and partial charge density distribution (PCDD) within the energy range of ($E_F - 0.1$ eV, E_F). Only slight differences of the PDOS around the E_F are observed between the normal and CDW phases, while complex patterns stemming from the periodic structural modulation merge in the PCDD of CDW phases [Figs. 5(k) and 5(l)]. Considering that the states near the E_F of VS₂ and VTe₂ are dominantly contributed by the dz^2 and $dx^2 - y^2$ orbitals, the PCDD illustrates the alignment of these orbitals for all V atoms in normal phase (Fig. S10). Such neat arrangement is broken in the $\sqrt{7} \times \sqrt{3}$ CDW phases of VS₂. Within any butterfly pattern, each pair of diagonal

V atoms exhibits aligned dz^2 orbitals, whereas each pair of neighboring V atoms possesses dz^2 orbitals with different orientations. In contrast, the orbital alignment is preserved in the 4×4 CDW phase of VTe₂, whereas the wave-function overlap between atoms in different strips is tiny due to the large distance [Fig. 5(l) and Table S1]. The above analyses indicate that the distinctions in conductivities mainly arise from the varying orientation and location distributions of relevant wave functions.

Conclusions. In conclusion, the fundamental mechanism of CDW phase transitions in VS₂ and VTe₂ monolayers was elucidated by DFT and machine-learning accelerated AIMD simulations. Electron-phonon coupling is demonstrated to be the main driving force of CDW transition, with the predicted T_{CDW} consistent with previous experiments. The presence of three-center bonds and enhanced p - d hybridization play a crucial role in the stability of CDW. Reversible transitions between the normal and CDW phases are observed during the cooling and heating processes with AIMD. The formation of CDW phase exhibits a rapid nucleation process involving the formation, flipping, translation, and aggregation of characteristic patterns. The fast structural evolution towards the CDW phase is strongly correlated with the soft phonon

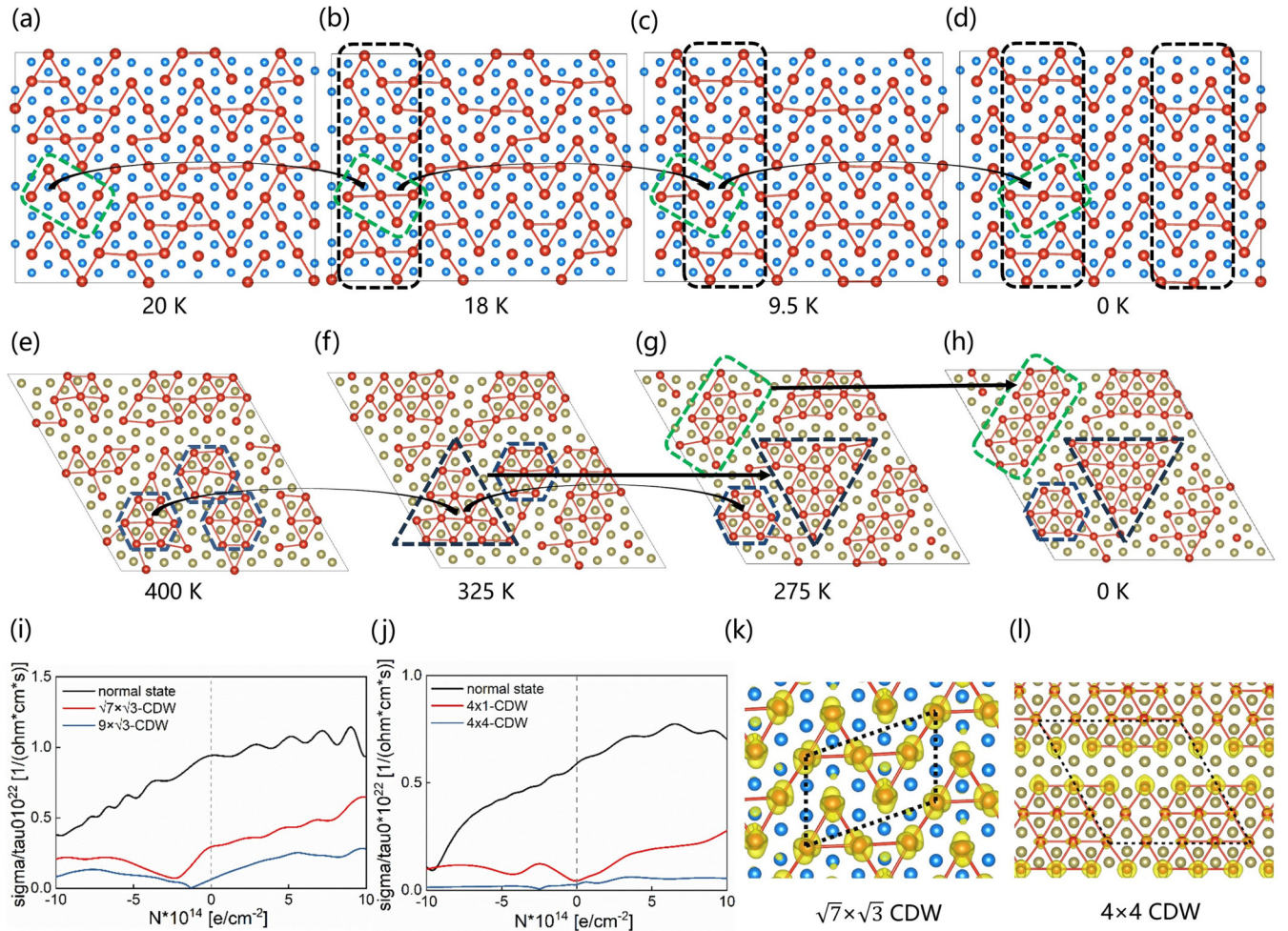


FIG. 5. Schematic illustration of CDW formation and its impact on transport property. Critical structural evolution during the AIMD cooling processes for (a)–(d) VS₂ and (e)–(h) VTe₂. Colored dashed shapes highlight the parts with significant structural changes. Comparison of electric conductivity at 300 K between the CDW and NS phases for (i) VS₂ and (j) VTe₂. Partial charge density distributions of (k) $\sqrt{7} \times \sqrt{3}$ CDW in VS₂ and (l) 4×4 CDW structures in VTe₂ within the energy range of $(E_F - 0.1 \text{ eV}, E_F)$. The value of the isosurface is set to $0.003 \text{ e}\text{\AA}^{-3}$.

modes. The distinct charge-transport property between normal and CDW phases is likely to arise from the varying orientation and location distributions of relevant wave functions. The microscopic dynamic analyses performed in this study can be generalized to any CDW transitions, which may provide valuable insights to the applications in logical circuits and neural networks.

Acknowledgments. The authors acknowledge the support from the National Natural Science Foundation of China

(Grants No. 52072417 and No. 11832019), the NSFC original exploration project (Grant No. 12150001), the Natural Science Foundation of Guangdong Province (Grant No. 2018B030306036), the Guangdong Science & Technology Project No. 2019QN01C113, and the Guangdong International Science and Technology Cooperation Program (Grant No. 2020A0505020005). This research used computational resources of the National Supercomputer Center in Guangzhou.

- [1] X. Zhu, Y. Cao, J. Zhang, E. W. Plummer, and J. Guo, Classification of charge density waves based on their nature, *Proc. Natl. Acad. Sci. USA* **112**, 2367 (2015).
- [2] D. Cho, G. Gye, J. Lee, S.-H. Lee, L. Wang, S.-W. Cheong, and H. W. Yeom, Correlated electronic states at domain walls of a mott-charge-density-wave insulator 1T-TaS₂, *Nat. Commun.* **8**, 392 (2017).
- [3] J.-J. Zhou, J. Park, I. Timrov, A. Floris, M. Cococcioni, N. Marzari, and M. Bernardi, Ab initio electron-phonon inter-

actions in correlated electron systems, *Phys. Rev. Lett.* **127**, 126404 (2021).

- [4] C. Park, Calculation of charge density wave phase diagram by interacting eigenmodes method, *J. Phys.: Condens. Matter* **34**, 315401 (2022).

- [5] X. Sun, X. Jiang, Z. Wang, X. Xu, L. Yang, Q. Gao, D. Li, B. Cui, and D. Liu, Spin transport properties of T-Phase VSe₂ 2D materials based on eight-atom-ring line defects, *Results Phys.* **49**, 106553 (2023).

- [6] Y. Bai *et al.*, Realization of multiple charge-density waves in NbTe₂ at the monolayer limit, *Nano Lett.* **23**, 2107 (2023).
- [7] R. Chua, J. Henke, S. Saha, Y. Huang, J. Gou, X. He, T. Das, J. van Wezel, A. Soumyanarayanan, and A. T. S. Wee, Coexisting charge-ordered states with distinct driving mechanisms in monolayer VSe₂, *ACS Nano* **16**, 783 (2022).
- [8] Y. W. Li, J. Jiang, H. F. Yang, D. Prabhakaran, Z. K. Liu, L. X. Yang, and Y. L. Chen, Folded superstructure and degeneracy-enhanced band gap in the weak-coupling charge density wave system 2H-TaSe₂, *Phys. Rev. B* **97**, 115118 (2018).
- [9] W. Shi *et al.*, A charge-density-wave topological semimetal, *Nat. Phys.* **17**, 381 (2021).
- [10] X. Wang, Z. Song, W. Wen, H. Liu, J. Wu, C. Dang, M. Hossain, M. A. Iqbal, and L. Xie, Potential 2D materials with phase transitions: structure, synthesis, and device applications, *Adv. Mater.* **31**, 1804682 (2019).
- [11] K. Sun, S. Sun, C. Zhu, H. Tian, H. Yang, and J. Li, Hidden CDW states and insulator-to-metal transition after a pulsed femtosecond laser excitation in layered chalcogenide 1T-TaS_{2-x}Se_x, *Sci. Adv.* **4**, eaas9660 (2018).
- [12] W. Wen, C. Dang, and L. Xie, Photoinduced phase transitions in two-dimensional charge-density-wave 1T-TaS₂, *Chin. Phys. B* **28**, 058504 (2019).
- [13] H. Tanimura, N. L. Okamoto, T. Homma, Y. Sato, A. Ishii, H. Takamura, and T. Ichitsubo, Nonthermal melting of charge density wave order via nucleation in VTe₂, *Phys. Rev. B* **105**, 245402 (2022).
- [14] H. J. Kim, Electronic structure and charge-density wave transition in monolayer VS₂, *Curr. Appl. Phys.* **30**, 8 (2021).
- [15] C. van Efferen *et al.*, A full gap above the fermi level: The charge density wave of monolayer VS₂, *Nat. Commun.* **12**, 6837 (2021).
- [16] P. M. Coelho, K. Lasek, K. Nguyen Cong, J. Li, W. Niu, W. Liu, I. I. Oleynik, and M. Batzill, Monolayer modification of VTe₂ and its charge density wave, *J. Phys. Chem. Lett.* **10**, 4987 (2019).
- [17] D. Wang, J. Wu, and C. Si, Emergence of charge density wave and ising superconductivity in centrosymmetric monolayer 1T-HfTe₂, *Nano Res.* **16**, 11521 (2023).
- [18] M. Liu, C. Wu, Z. Liu, Z. Wang, D.-X. Yao, and D. Zhong, Multimorphism and gap opening of charge-density-wave phases in monolayer VTe₂, *Nano Res.* **13**, 1733 (2020).
- [19] T. Kawakami, K. Sugawara, H. Oka, K. Nakayama, K. Yaegashi, S. Souma, T. Takahashi, T. Fukumura, and T. Sato, Charge-density wave associated with higher-order fermi-surface nesting in monolayer VS₂, *npj 2D Mater. Appl.* **7**, 1 (2023).
- [20] Z.-L. Zhu *et al.*, Charge density wave states in phase-engineered monolayer VTe₂, *Chin. Phys. B* **31**, 077101 (2022).
- [21] K. Sugawara, Y. Nakata, K. Fujii, K. Nakayama, S. Souma, T. Takahashi, and T. Sato, Monolayer VTe₂: Incommensurate fermi surface nesting and suppression of charge density waves, *Phys. Rev. B* **99**, 241404(R) (2019).
- [22] M. D. Johannes, I. I. Mazin, and C. A. Howells, Fermi-surface nesting and the origin of the charge-density wave in NbSe₂, *Phys. Rev. B* **73**, 205102 (2006).
- [23] Z. Wang, C. Chen, J. Mo, J. Zhou, K. P. Loh, and Y. P. Feng, Decisive role of electron-phonon coupling for phonon and electron instabilities in transition metal dichalcogenides, *Phys. Rev. Res.* **5**, 013218 (2023).
- [24] M. Calandra and F. Mauri, Charge-density wave and superconducting dome in TiSe₂ from electron-phonon interaction, *Phys. Rev. Lett.* **106**, 196406 (2011).
- [25] Z. Wang, J.-Y. You, C. Chen, J. Mo, J. He, L. Zhang, J. Zhou, K. Ping Loh, and Y. Ping Feng, Interplay of the charge density wave transition with topological and superconducting properties, *Nanoscale Horiz.* **8**, 1395 (2023).
- [26] J. Zhou, Z. Wang, S. Wang, Y. P. Feng, M. Yang, and L. Shen, Coexistence of ferromagnetism and charge density waves in monolayer LaBr₂, *Nanoscale Horiz.* **8**, 1054 (2023).
- [27] Z. Wang, J. Zhou, K. P. Loh, and Y. P. Feng, Controllable phase transitions between multiple charge density waves in monolayer 1T-VSe₂ via charge doping, *Appl. Phys. Lett.* **119**, 163101 (2021).
- [28] Y. S. Oh, J. J. Yang, Y. Horibe, and S.-W. Cheong, Anionic depolymerization transition in IrTe₂, *Phys. Rev. Lett.* **110**, 127209 (2013).
- [29] G. Saleh and S. Artyukhin, First-principles theory of phase transitions in IrTe₂, *J. Phys. Chem. Lett.* **11**, 2127 (2020).
- [30] T. Ritschel, Q. Stahl, M. Kusch, J. Trinckauf, G. Garbarino, V. Svitlyk, M. Mezouar, J. Yang, S.-W. Cheong, and J. Geck, Stabilization mechanism of molecular orbital crystals in IrTe₂, *Commun. Phys.* **5**, 1 (2022).
- [31] J. van Landuyt, G. A. Wieggers, and S. Amelinckx, A new type of deformation modulated superstructure in 1T-VSe₂ and its relation with other superstructures in transition metal dichalcogenides, *Phys. Status Solidi A* **46**, 479 (1978).
- [32] K. Stolze, A. Isaeva, F. Nitsche, U. Burkhardt, H. Lichte, D. Wolf, and T. Doert, CuTe: Remarkable bonding features as a consequence of a charge density wave, *Angew. Chem. Int. Ed.* **52**, 862 (2013).
- [33] N. Katayama *et al.*, Large entropy change derived from orbitally assisted three-centered two-electron σ bond formation in metallic Li_{0.33}VS₂, *Phys. Rev. B* **98**, 081104(R) (2018).
- [34] J. Zhang, C. Lian, M. Guan, W. Ma, H. Fu, H. Guo, and S. Meng, Photoexcitation induced quantum dynamics of charge density wave and emergence of a collective mode in 1T-TaS₂, *Nano Lett.* **19**, 6027 (2019).
- [35] D. G. Trabada, DFT molecular dynamics and free energy analysis of a charge density wave surface system, *Appl. Surf. Sci.* **479**, 260 (2019).
- [36] Y. Zheng, X. Jiang, X.-X. Xue, X. Yao, J. Zeng, K.-Q. Chen, E. Wang, and Y. Feng, Nuclear quantum effects on the charge-density wave transition in NbX₂ (X = S, Se), *Nano Lett.* **22**, 1858 (2022).
- [37] S. Chowdhury, A. F. Rigosi, H. M. Hill, P. Vora, A. R. Hight Walker, and F. Tavazza, Computational methods for charge density waves in 2D materials, *Nanomaterials* **12**, 504 (2022).
- [38] Z. Xu *et al.*, Topical review: recent progress of charge density waves in 2D transition metal dichalcogenide-based heterojunctions and their applications, *Nanotechnology* **32**, 492001 (2021).
- [39] P. Liu, C. Verdi, F. Karsai, and G. Kresse, Phase transitions of zirconia: machine-learned force fields beyond density functional theory, *Phys. Rev. B* **105**, L060102 (2022).
- [40] P. Liu, C. Verdi, F. Karsai, and G. Kresse, α - β phase transition of zirconium predicted by on-the-fly machine-learned force field, *Phys. Rev. Mater.* **5**, 053804 (2021).

- [41] A. G. Khitun, A. K. Geremew, and A. A. Balandin, Transistorless logic circuits implemented with 2-D charge density wave devices, *IEEE Electron Device Lett.* **39**, 1449 (2018).
- [42] H. Duan, S. Cheng, L. Qin, X. Zhang, B. Xie, Y. Zhang, and W. Jie, Low-power memristor based on two-dimensional materials, *J. Phys. Chem. Lett.* **13**, 7130 (2022).
- [43] A. Khitun, G. Liu, and A. A. Balandin, Two-dimensional oscillatory neural network based on room-temperature charge-density-wave devices, *IEEE Trans. Nanotechnol.* **16**, 860 (2017).
- [44] B. Burk, R. E. Thomson, J. Clarke, and A. Zettl, Surface and bulk charge density wave structure in 1T-TaS₂, *Science* **257**, 362 (1992).
- [45] A. Fang, N. Ru, I. R. Fisher, and A. Kapitulnik, STM studies of TbTe₃: Evidence for a fully incommensurate charge density wave, *Phys. Rev. Lett.* **99**, 046401 (2007).
- [46] See Supplemental Material at <http://link.aps.org/supplemental/10.1103/PhysRevB.109.L140105> for Computational method details; Influence of SOC and U on electronic bands and phonon spectra; Schematics of CDW structures; Unfolded band structures; Computational analyses of multicenter bonding; p - d orbital hybridization; CDW atomic structures; Initial structure and mechanical strain impacts on CDW transitions; Comparison of electric conductivity and partial charge density distribution; and PDOS of V $3d$ electron orbits. The table lists lattice constants, angles, and bond lengths for various periodicities. The Supplemental Material also contains Refs. [47–73].
- [47] J. Hempelmann, P. C. Müller, C. Ertural, and R. Dronskowski, The orbital origins of chemical bonding in Ge–Sb–Te phase-change materials, *Angew. Chem. Int. Ed.* **61**, e202115778 (2022).
- [48] K. Beuthert, F. Pan, L. Guggolz, R. J. Wilson, J. Hempelmann, R. Dronskowski, and S. Dehnen, Between elemental match and mismatch: from K₁₂Ge_{3.5}Sb₆ to salts of (Ge₂Sb₂)²⁻, (Ge₄Sb₁₂)⁴⁻, and (Ge₄Sb₁₄)⁴⁻, *Angew. Chem.* **134**, e202207232 (2022).
- [49] A. Jain *et al.*, Commentary: The materials project: a materials genome approach to accelerating materials innovation, *APL Mater.* **1**, 011002 (2013).
- [50] S. Poncé, E. R. Margine, C. Verdi, and F. Giustino, EPW: Electron–phonon coupling, transport and superconducting properties using maximally localized wannier functions, *Comput. Phys. Commun.* **209**, 116 (2016).
- [51] V. Wang, N. Xu, J.-C. Liu, G. Tang, and W.-T. Geng, VASPKIT: A user-friendly interface facilitating high-throughput computing and analysis using VASP code, *Comput. Phys. Commun.* **267**, 108033 (2021).
- [52] Y. Cui, W. Fan, X. Liu, J. Ren, and Y. Gao, Electronic conductivity of two-dimensional VS₂ monolayers: A first principles study, *Comput. Mater. Sci.* **200**, 110767 (2021).
- [53] G. Kresse and J. Furthmüller, Efficiency of ab-initio total energy calculations for metals and semiconductors using a plane-wave basis set, *Comput. Mater. Sci.* **6**, 15 (1996).
- [54] J.-H. Liao, Y.-C. Zhao, Y.-J. Zhao, X.-B. Yang, and Y. Chen, Doping induced charge density wave in monolayer TiS₂ and phonon-mediated superconductivity, *J. Appl. Phys.* **127**, 044301 (2020).
- [55] T. Tsuda, H. Yasuoka, Y. Kitaoka, and F. J. Di Salvo, 51V NMR study of the phase transition in 1T-VS₂, *J. Magn. Magn. Mater.* **31–34**, 1101 (1983).
- [56] P. C. Müller, C. Ertural, J. Hempelmann, and R. Dronskowski, Crystal orbital bond index: Covalent bond orders in solids, *J. Phys. Chem. C* **125**, 7959 (2021).
- [57] P. Giannozzi *et al.*, QUANTUM ESPRESSO: A modular and open-source software project for quantum simulations of materials, *J. Phys.: Condens. Matter* **21**, 395502 (2009).
- [58] M. Kan, B. Wang, Y. H. Lee, and Q. Sun, A density functional theory study of the tunable structure, magnetism and metal-insulator phase transition in VS₂ monolayers induced by in-plane biaxial strain, *Nano Res.* **8**, 1348 (2015).
- [59] G. A. Wiegers, Physical properties of first-row transition metal dichalcogenides and their intercalates, *Physica B+C* **99**, 151 (1980).
- [60] M. Aras, Ç. Kılıç, and S. Ciraci, Magnetic ground state in FeTe₂, VS₂, and NiTe₂ monolayers: Antiparallel magnetic moments at chalcogen atoms, *Phys. Rev. B* **101**, 054429 (2020).
- [61] P. E. Blöchl, Projector augmented-wave method, *Phys. Rev. B* **50**, 17953 (1994).
- [62] G. Kresse and J. Furthmüller, Efficient iterative schemes for *Ab Initio* total-energy calculations using a plane-wave basis set, *Phys. Rev. B* **54**, 11169 (1996).
- [63] B. Hammer, L. B. Hansen, and J. K. Nørskov, Improved adsorption energetics within density-functional theory using revised perdew-burke-ernzerhof functionals, *Phys. Rev. B* **59**, 7413 (1999).
- [64] F. Giustino, M. L. Cohen, and S. G. Louie, Electron-phonon interaction using wannier functions, *Phys. Rev. B* **76**, 165108 (2007).
- [65] M. Mulazzi *et al.*, Absence of nesting in the charge-density-wave system 1T-VS₂ as seen by photoelectron spectroscopy, *Phys. Rev. B* **82**, 075130 (2010).
- [66] D. R. Hamann, Optimized norm-conserving vanderbilt pseudopotentials, *Phys. Rev. B* **88**, 085117 (2013).
- [67] H. L. Zhuang and R. G. Hennig, Stability and magnetism of strongly correlated single-layer VS₂, *Phys. Rev. B* **93**, 054429 (2016).
- [68] E. B. Isaacs and C. A. Marianetti, Electronic correlations in monolayer VS₂, *Phys. Rev. B* **94**, 035120 (2016).
- [69] W.-M. Zhao, W. Ding, Q.-W. Wang, Y.-X. Meng, L. Zhu, Z.-Y. Jia, W. Zhu, and S.-C. Li, Observation of electronic strong correlation in VT₂-2√3×2√3 monolayer, *Phys. Rev. Lett.* **131**, 086501 (2023).
- [70] J. P. Perdew, K. Burke, and M. Ernzerhof, Generalized gradient approximation made simple, *Phys. Rev. Lett.* **77**, 3865 (1996).
- [71] M. Dion, H. Rydberg, E. Schröder, D. C. Langreth, and B. I. Lundqvist, Van der Waals density functional for general geometries, *Phys. Rev. Lett.* **92**, 246401 (2004).
- [72] A. Togo and I. Tanaka, First principles phonon calculations in materials science, *Scr. Mater.* **108**, 1 (2015).
- [73] E. Canadell, S. Jobic, R. Brec, J. Rouxel, and M.-H. Whangbo, Importance of short interlayer Te...Te contacts for the structural distortions and physical properties of CdI₂ type layered transition-metal ditellurides, *J. Solid State Chem.* **99**, 189 (1992).
- [74] J. G. Si, W. J. Lu, H. Y. Wu, H. Y. Lv, X. Liang, Q. J. Li, and Y. P. Sun, Origin of the multiple charge density wave order in 1T-VSe₂, *Phys. Rev. B* **101**, 235405 (2020).
- [75] J. Diego, A. H. Said, S. K. Mahatha, R. Bianco, L. Monacelli, M. Calandra, F. Mauri, K. Rossnagel, I. Errea, and

- S. Blanco-Canosa, van der Waals driven anharmonic melting of the 3D charge density wave in VSe_2 , *Nat. Commun.* **12**, 598 (2021).
- [76] D. L. Duong, M. Burghard, and J. C. Schön, Ab initio computation of the transition temperature of the charge density wave transition in TiSe_2 , *Phys. Rev. B* **92**, 245131 (2015).
- [77] J. S. Zhou, L. Monacelli, R. Bianco, I. Errea, F. Mauri, and M. Calandra, Anharmonicity and doping melt the charge density wave in single-layer TiSe_2 , *Nano Lett.* **20**, 4809 (2020).
- [78] A. Togo, First-principles phonon calculations with phonopy and phono3py, *J. Phys. Soc. Jpn.* **92**, 012001 (2023).
- [79] A. Carreras, A. Togo, and I. Tanaka, DynaPhoPy: A code for extracting phonon quasiparticles from molecular dynamics simulations, *Comput. Phys. Commun.* **221**, 221 (2017).
- [80] X. Ma *et al.*, Charge density wave phase transitions in large-scale few-layer 1T-VTe₂ grown by molecular beam epitaxy, *ACS Appl. Mater. Interfaces* **11**, 10729 (2019).
- [81] M. D. Johannes and I. I. Mazin, Fermi surface nesting and the origin of charge density waves in metals, *Phys. Rev. B* **77**, 165135 (2008).
- [82] A. O. Fumega, J. Diego, V. Pardo, S. Blanco-Canosa, and I. Errea, Anharmonicity reveals the tunability of the charge density wave orders in monolayer VSe_2 , *Nano Lett.* **23**, 1794 (2023).
- [83] L. Yin, T. Berlijn, R. Juneja, L. Lindsay, and D. S. Parker, Competing magnetic and nonmagnetic states in monolayer VSe_2 with charge density wave, *Phys. Rev. B* **106**, 085117 (2022).
- [84] J. Hall *et al.*, Environmental control of charge density wave order in monolayer 2H-TaS₂, *ACS Nano* **13**, 10210 (2019).
- [85] S. Kolekar, M. Bonilla, H. C. Diaz, M. Hashimoto, D. Lu, and M. Batzill, Controlling the charge density wave transition in monolayer TiSe_2 : Substrate and doping effects, *Adv. Quantum Technol.* **1**, 1800070 (2018).
- [86] J. K. Burdett and T. Hughbanks, Aspects of metal-metal bonding in early-transition-metal dioxides, *Inorg. Chem.* **24**, 1741 (1985).
- [87] M. H. Whangbo and E. Canadell, Analogies between the concepts of molecular chemistry and solid-state physics concerning structural instabilities. Electronic origin of the structural modulations in layered transition metal dichalcogenides, *J. Am. Chem. Soc.* **114**, 9587 (1992).
- [88] D. I. Khomskii and T. Mizokawa, Orbitally induced peierls state in spinels, *Phys. Rev. Lett.* **94**, 156402 (2005).
- [89] S. Kim, B. Kim, and K. Kim, Role of coulomb correlations in the charge density wave of CuTe , *Phys. Rev. B* **100**, 054112 (2019).
- [90] J. Dai, E. Calleja, J. Alldredge, X. Zhu, L. Li, W. Lu, Y. Sun, T. Wolf, H. Berger, and K. McElroy, Microscopic evidence for strong periodic lattice distortion in two-dimensional charge-density wave systems, *Phys. Rev. B* **89**, 165140 (2014).
- [91] G. K. H. Madsen, J. Carrete, and M. J. Verstraete, BoltzTraP2, a program for interpolating band structures and calculating semiclassical transport coefficients, *Comput. Phys. Commun.* **231**, 140 (2018).
- [92] X. Sun, T. Yao, Z. Hu, Y. Guo, Q. Liu, S. Wei, and C. Wu, In situ unravelling structural modulation across the charge-density-wave transition in vanadium disulfide, *Phys. Chem. Chem. Phys.* **17**, 13333 (2015).